# An improved simulation methodology for nanoparticle injection through aerodynamic lens systems

Surya Kiran Peravali ⓘ ; Amit K. Samanta ⓘ ; Muhamed Amin ⓘ ; Philipp Neumann ⓘ ; Jochen Küpper ⓘ ;
Michael Breuer ✉ ⓘ

Check for updates

View
Online

Export
Citation

**Articles You May Be Interested In**

KoopmanLab: Machine learning for solving complex physics equations

*APL Mach. Learn.* (September 2023)

Experimental realization of a quantum classification: Bell state measurement via machine learning

*APL Mach. Learn.* (September 2023)
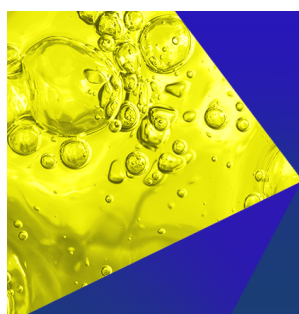
# An improved simulation methodology for nanoparticle injection through aerodynamic lens systems

View Online        Export Citation        CrossMark

Surya Kiran Peravali,[1,2,a]  (iD)  Amit K. Samanta,[2,3]  (iD)  Muhamed Amin,[2,4]  (iD)  Philipp Neumann,[5,6]  (iD)
Jochen Küpper,[2,3,7]  (iD)  and Michael Breuer[1,b]  (iD)

**AFFILIATIONS**

[1]Professur für Strömungsmechanik, Helmut-Schmidt-Universität/Universität der Bundeswehr Hamburg, 22043 Hamburg, Germany
[2]Center for Free-Electron Laser Science CFEL, Deutsches Elektronen-Synchrotron DESY, Notkestr. 85, 22607 Hamburg, Germany
[3]Center for Ultrafast Imaging, Universität Hamburg, Luruper Chaussee 149, 22761 Hamburg, Germany
[4]Laboratory of Computational Biology, National Heart, Lung and Blood Institute, National Institutes of Health,
 Bethesda, Maryland 20892, USA
[5]Department of Informatics, High Performance Computing & Data Science, Universität Hamburg, 22603 Hamburg, Germany
[6]Deutsches Elektronen-Synchrotron DESY, Notkestr. 85, 22607 Hamburg, Germany
[7]Department of Physics, Universität Hamburg, Luruper Chaussee 149, 22761 Hamburg, Germany

[a]Electronic mail: peravals@hsu-hh.de; **URL:** https://www.controlled-molecule-imaging.org
[b]Author to whom correspondence should be addressed: breuer@hsu-hh.de

**ABSTRACT**

Aerosol injectors applied in single-particle diffractive imaging experiments demonstrated their potential in efficiently delivering nanoparticles with high density. Continuous optimization of injector design is crucial for achieving high-density particle streams, minimizing background gas, enhancing x-ray interactions, and generating high-quality diffraction patterns. We present an updated simulation framework designed for the fast and effective exploration of the experimental parameter space to enhance the optimization process. The framework includes both the simulation of the carrier gas and the particle trajectories within injectors and their expansion into the experimental vacuum chamber. A hybrid molecular-continuum-simulation method [direct simulation Monte Carlo (DSMC)/computational fluid dynamics (CFD)] is utilized to accurately capture the multi-scale nature of the flow. The simulation setup, initial benchmark results of the coupled approach, and the validation of the entire methodology against experimental data are presented. The results of the enhanced methodology show a significant improvement in the prediction quality compared to previous approaches.

## I. INTRODUCTION

Single-particle diffractive imaging (SPI) is a novel technique used for imaging atomic-scale structures ranging from few micrometers to nanometers,[1,2] such as bio-molecules, proteins or artificial nanoparticles. In this approach, identical particles are delivered in a high-density stream into vacuum where they are intersected with x-ray free-electron laser (XFEL) pulses. When an x-ray pulse hits the particle in flight, a two-dimensional diffraction pattern is produced. Collecting a large set of such diffraction patterns of identical particles, allows for the reconstruction of the particles three-dimensional structure.[3–5] Particles that interacted with the intense x-ray pulses are destroyed.

Therefore, a continuous stream of identical particles is required, which can be achieved using aerosol injectors. Aerodynamic-lens-stack (ALS) injectors are most commonly used at XFEL facilities to provide focused or collimated nanoparticle beams for SPI experiments.[3,6]

An ALS consists of a series of orifices, traversed by the particles in the gas phase, from which a particle stream is extracted into the vacuum. The typical design and setup of an ALS in an SPI experiment were described elsewhere.[7] The sample-injection system must be optimized in order to produce high-quality particle beams, i.e., a high particle density to increase the hit rate with the x-ray pulse and a low carrier gas density to reduce background scattering.[7] The latter

26 March 2025 12:04:40

necessitates shifting the particle-beam focus away from the ALS exit. Optimizing the ALS design based on experimental characterization in its large parameter space is time-consuming and thus often impractical. A computational approach can serve as a fast and efficient alternative to investigate the parameters, e.g., flow rate, pressure, and carrier gas, that control the particle-beam size and the focusing behavior.

Single and multi-lens systems for particle beam collimation by an ALS were characterized utilizing numerical simulations.[8,9] A numerical study described the focusing of particles to a beam with a diameter smaller than 30 nm using an ALS.[10,11] This work established the guidelines for designing aerodynamic lens systems for nanoparticles and also a design tool that predicts ALS dimensions to focus particles of certain sizes at different flow conditions.[12] However, in all these studies, the flow through the ALS was assumed to be a *continuum* as numerical solvers based on continuum mechanics, i.e., the Navier–Stokes equations, were used to predict the gas flows. In the design of an ALS, the flow is always constrained to be laminar because flow instabilities and turbulence can disperse particles and destroy focusing.[12] Particle trajectories were computed based on forces determined from these simulated flow fields. This numerical methodology was adopted for simulating nanoparticle-injection experiments at XFEL facilities,[13] which further led to the development of an in-house particle trajectory simulation tool denoted CMInject.[14] Here, the drag force model used for calculating the particle movement in the fluid is described by Stokes' law. While the flow field is in the continuum range in these specific cases, non-continuum effects prevail with respect to the small particles as in certain cases the particle diameters can be smaller than the mean-free path of the fluid (Knudsen number $Kn_p > 1$) leading to decreased drag forces. To take this into account, the empirical Cunningham slip-correction factor[15] was used along with the Stokes drag. Additionally, a Brownian-motion force was added to the drag term in order to incorporate the Brownian motion of the nanoparticles.

The nanoparticle focusing behavior in multi-scale flow regimes, i.e., transition and free-molecular flow regime, is largely unexplored.[10] In these regimes, the flow Knudsen number $Kn$ has a large value ($Kn > 0.1$), such that the continuum assumption for the flow is violated. Therefore, traditional Navier–Stokes-based computational fluid dynamics (CFD) solvers fail to accurately resolve the flow, and particle-based Boltzmann solvers, such as direct simulation Monte Carlo (DSMC), have become the method of choice. However, the DSMC method is challenging if the simulation includes both continuum and rarefied regions. Furthermore, this method is computationally very inefficient for small Knudsen numbers ($Kn < 0.1$). This necessitates the use of a hybrid approach combining DSMC with CFD. The review of this methodology and its applicability to various rarefied flow problems, such as microfluidic devices, vacuum technology, spacecraft thruster design, and space applications, such as reentry flows, are discussed in detail in a previous work.[16]

The Stokes–Cunningham drag model described and used in previous numerical works[8–11,13,14] is confined to continuum gas flow fields at low Mach numbers and strictly depends on empirical relations. For rarefied flow regimes ($Kn_p > 1$), the drag force on spherical particles at small Mach numbers was described by the Epstein model.[17] Unlike the Cunningham model, which assumes the gas molecules to be specularly reflected on the surface of the sphere, the Epstein drag model assumes a combination of both specular and diffusive gas–surface

collisions. A closed-form of expression for the drag force on small spheres in the free-molecular regime for all Mach numbers was described.[18] Furthermore, several studies reported on the generalization of the drag force model to encompass a broad spectrum of Reynolds and Mach numbers. These works relied on either *ad hoc* interpolations between different regimes,[19,20] empirical correlations from the available literature[21] or neural-network based empirical formulations.[22] In recent years, a derivation of a generalized physics-based expression for the drag coefficient of spherical particles was attempted.[23] For highly rarefied regimes where gas can tend toward non-equilibrium, a DSMC based approach for computing force on a particle was introduced.[24,25] This is advantageous where the molecular distribution of the gas is not known beforehand and can only be determined through DSMC computations. The main disadvantages of this model are that it can be inaccurate in the low Knudsen number regime and it is computationally inefficient.

The research question of this study is how to develop a suitable simulation methodology that allows to predict particle trajectories in ALS systems within a wide parameter range with an accuracy that allows optimization of the system. For this purpose, we present a new, improved simulation framework utilizing a one-way coupled CFD–DSMC methodology to resolve the gas flow through ALS systems in the presence of different Knudsen number regimes. This hybrid CFD–DSMC methodology was already validated[16] based on a gasdynamic nozzle case.[26] Here, the motion of the nanoparticles through the multi-scale ALS flow is modeled and the particle interaction with the background gas is examined. The accuracy of the entire simulation tool is evaluated by comparing the simulations with experimental data.[27] Finally, the nanoparticle-focusing behavior through the ALS is studied in detail based on the improved simulation framework along with additional corrections of the molecular drag models[17,18] at extremely rarefied flow conditions.

## II. TEST CASE AND EXPERIMENTATION

The nanoparticle beams were generated using the experimental setup shown in Fig. 1. Polystyrene spheres (PS) were aerosolized at pressures of about $10^5$ Pa and passed through a differentially-pumped skimmer assembly to reduce gas-load and pressure in the experiment.
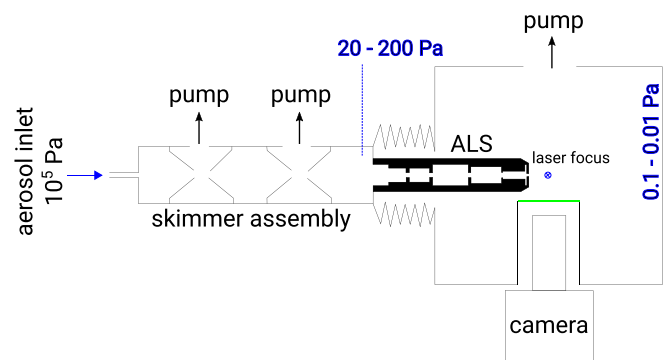


**FIG. 1.** Schematic of a typical experimental setup used in the particle-beam evolution measurements.[27] The setup consists of a double skimmer setup with adjustable pumping, an aerodynamic-lens-stack assembly for particle-beam generation, and the optical scattering setup and particle-localization microscopy inside a high-vacuum chamber.

The particles were focused through an ALS into the ultra-high vacuum detection chamber ($p \approx 10^{-1}$ Pa). These experiments were carried out for different ALS inlet-gas pressures ($p_{in}$) and different particle sizes summarized in Table I along with the flow Knudsen numbers ($Kn$) and particle Knudsen numbers ($Kn_p$) at the inlet of the ALS.

It can be seen that for the particle size of 25 nm, the experiments were conducted at different inlet pressures compared to the particles sizes 69 and 42 nm. This difference is due to the higher divergence of the 25 nm particle beam at pressures below 50 Pa, where reliable data could not be collected. For this reason, experiments with these smaller nanoparticles ($\leq 25$ nm) were carried out over a higher pressure range than those with larger particles.[27]

The particle beam profiles were obtained through particle-localization microscopy[28] at different distances from the exit of the ALS. Detailed descriptions of the ALS geometry used in the experiment, the experimental procedure, and the analysis of the experimental data were described elsewhere.[27]

## III. SIMULATION METHODOLOGY

In the described experiments, the volume fraction of the particles in the gas–particle mixture was very low. Therefore, it is assumed that the particles do not influence the flow field of the gas and t there is no, or only negligible interaction between the particles. This implies that the gas–particle dynamics can be calculated in a decoupled manner, and we employ a two-step approach to calculate the gas–particle dynamics: First, we calculate the flow field through the ALS, which is converged to a steady-state solution. Second, the particles are tracked independently by interpolating the forces obtained from the flow field. We utilize various methods for resolving the fluid field in different regimes, which are described in subsections III A–III C. Furthermore, different models for the forces that influence the particle transport are described in Sec. III D.

### A. Flow field in continuum (CFD)

For the experiments with higher inlet pressures, i.e., when the Knudsen numbers $Kn$ of the flow field throughout the ALS and near its exit are small ($Kn < 0.1$), the flow can be described as continuum ($0 < Kn < 0.01$) or in a slip regime ($0.01 < Kn < 0.1$). For these regimes, the flow field can be computed by solving the Navier–Stokes equations. The continuum gas flow field is computed using the finite-volume software OpenFOAM.[29] Since the flow through the ALS transits from subsonic to supersonic speeds in the streamwise direction,

**TABLE I.** Gas-flow and particle parameters of the experiments.

| Particle size (nm) | Inlet pressure, $p_{in}$ (Pa) | $Kn$ | $Kn_p$ |
|---|---|---|---|
| 69 | 180 | 0.0241 | 523.87 |
| | 55 | 0.0788 | 1714.50 |
| | 20 | 0.2168 | 4714.88 |
| 42 | 180 | 0.0241 | 860.65 |
| | 55 | 0.0788 | 2816.68 |
| | 20 | 0.2168 | 7745.87 |
| 25 | 200 | 0.0213 | 1279.196 |
| | 150 | 0.0289 | 1735.075 |
| | 50 | 0.0860 | 5205.225 |

the flow has to be assumed as compressible. A density-based transient solver (rhoCentralFoam) is utilized. Detailed information on the solver settings, e.g., discretization, interpolation, and algorithms can be found in a previous work.[16] The boundary conditions for the simulation cases are presented in subsection 1 of Appendix B. Since in this case the Reynolds number is very low ($Re < 10$), the flow is assumed to be laminar and thus, a turbulence model is not required. Furthermore, the equation of state for a perfect gas was applied. The transport properties are estimated using the Sutherland transport model.[30] The CFD calculations of the test cases rely on the structured grid specified and depicted in subsection 1 of Appendix B. Numerical convergence is ensured by monitoring key parameters, such as pressure, velocity, and temperature – until they reach a steady state during the transient simulation.

### B. Highly rarefied flow (DSMC)

The pressure at the inlet of the ALS is one of the major tuning factors of particle injection in SPI experiments. Sometimes, very low inlet pressures $p_{in} < 50$ Pa are used to reduce the background x-ray scattering. For such low pressures, the gas flow corresponds to a large mean free path between gas molecules, and the Knudsen number is larger than 0.1. Pure CFD simulations cannot capture the flow physics of such a rarefied gas. To resolve the flow field in these regimes, the direct simulation Monte Carlo (DSMC) method is often a good choice.[31] It is a stochastic technique, which provides an approximate solution to the Boltzmann equation (1)

$$\frac{\partial f}{\partial t} + \mathbf{u} \cdot \nabla f = \left(\frac{\partial f}{\partial t}\right)_{\text{coll}}. \tag{1}$$

Here, any external forces are assumed to be negligible. Each simulation particle represents a large number of real gas molecules, maintaining the phase space of the overall distribution. The momentum term ($\mathbf{u} \cdot \nabla f$) and the collision term $\left(\frac{\partial f}{\partial t}\right)_{\text{coll}}$ are solved in a decoupled manner. The probabilistic models are utilized to solve the collision term and the relaxation of internal degrees of freedom. In this work, we used the DSMC software SPARTA (Stochastic PArallel Rarefied-gas Time-accurate Analyzer).[32] The DSMC solution is sensitive to several parameters, such as the number of simulation particles, the grid size of the computational domain, the time step, the inter-molecular/surface collision models, and the sampling. The ideal choice of these parameters depends on various other factors, such as operating conditions, Reynolds number, and gas/mixture properties. A variety of such options in SPARTA were evaluated in terms of the accuracy and performance of the solution,[16] including analyses on error estimation and uncertainty quantification. These evaluations established guidelines for accurate and efficient DSMC simulations, which are incorporated in the present study and noted in subsection 2 of Appendix B.

### C. Hybrid CFD–DSMC

The DSMC method has been demonstrated to have the capability of resolving rarefied flows. However, for low Knudsen number flows, this approach is computationally very expensive due to a drastic increase in collisions between the molecules. Furthermore, a large number of simulations must be carried out to filter out the statistical noise, which is observed particularly in the low-speed regions of the flow. As described earlier, the Navier–Stokes solution has always been

a better choice in this regime both in terms of accuracy and efficiency. For experiments with intermediate pressures at the ALS inlet, i.e., $50\,\mathrm{Pa} \leq p_{in} \leq 180\,\mathrm{Pa}$, it was observed that the flow through the ALS has a variable Knudsen number regime, i.e., it changes from continuum to transition and free-molecular-flow regime. Therefore, we setup a coupled CFD–DSMC approach for resolving such flows. The flow is initially simulated using CFD (Navier–Stokes equation) and a continuum breakdown criterion is evaluated. Based on this criterion, the former computational domain is split into CFD and DSMC regions using an interface. At this interface, the CFD solution data (flow variables) are interpolated and these interpolated data are used to generate the required inflow molecular flux per unit time[31] for the DSMC domain to carry out the DSMC simulation in the rarefied region. The DSMC solution is sampled to extract macroscopic information, e.g., velocity, pressure, and temperature, of the flow and the statistical noise is filtered out. The steady-state solution of the flow from both CFD, with a body-fitted grid, and DSMC, with a Cartesian grid, in their specific regions are then interpolated together on a regular Cartesian grid, see Fig. 2, to have a smoothed contiguous multi-scale flow field. This one-way coupled hybrid method was validated on a gasdynamic nozzle and compared with experimental data. The results of the hybrid method showed higher accuracy and computational efficiency than the pure DSMC method.[16] In summary, the hybrid method provides a balanced compromise between computational efficiency and achievable accuracy.

To estimate the continuum breakdown criterion in this approach, two different definitions of the Knudsen number are utilized: (a) Global Knudsen number $Kn$; (b) Local or Boyd's gradient length Knudsen number $Kn_{GLL,Q}$[33]

$$Kn = \frac{\lambda}{L}; \quad Kn_{GLL,Q} = \frac{\lambda|\nabla Q|}{Q}. \tag{2}$$

Here, $\lambda$ represents the mean free path of the gas, $L$ is the characteristic length scale, $Q$ represents a macroscopic flow property such as the density $\rho$, the velocity $\mathbf{v}$ or the temperature $T$. The breakdown parameter $Kn_B$ is estimated based on the maximum of the global and local Knudsen numbers over the computational domain and is compared to a threshold limit of 0.05.[34–36] If the value of $Kn_B$ gets larger than this limit, the region is dedicated to DSMC.

$$Kn_B = \max(Kn, Kn_{GLL,\rho}, Kn_{GLL,T}, Kn_{GLL,|\mathbf{v}|}). \tag{3}$$

### D. Particle transport

Particle trajectories are calculated using the Langevin approach where the forces on the nanoparticles are computed as the sum of the drag force $\mathbf{F}_{\mathrm{drag}}$ and the Brownian motion force $\mathbf{F}_b$

$$\frac{d}{dt}(m_p\,\mathbf{u}_p) = \mathbf{F}_{\mathrm{drag}} + \mathbf{F}_b \tag{4}$$

with the mass of the particle $m_p$, the particle velocity vector $\mathbf{u}_p$, and time $t$, respectively. Here, a one-way coupling of the particulate phase with the fluid phase, where the fluid forces on the particles are predicted based on the flow field but the flow field itself is not influenced by the particles, is sufficient due to the low volume fractions,[37] that allows to ignore particle–particle collisions[38] and simplifies the simulation procedure. In subsections III D 1–III D 3, different models for the drag force and the Brownian motion (Sec. III D 4) are described.

### 1. Stokes–Cunnningham drag model

The conventional Stokes drag is corrected by the Cunningham slip coefficient $(C_c)$[15]
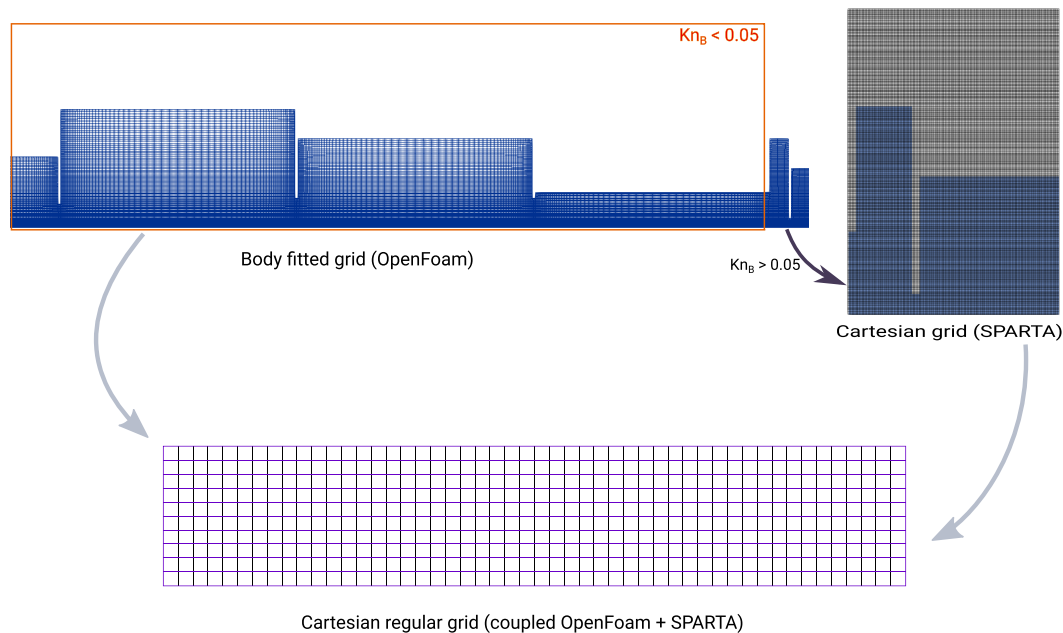


FIG. 2. Schematic diagram showing the hybrid CFD/DSMC coupling.

26 March 2025 12:04:40

$$\mathbf{F}_{\text{drag}} = \frac{6\pi \mu r_p \Delta\mathbf{U}}{C_c} \qquad (5)$$

with

$$C_c = 1 + Kn_p \left[ A_1 + A_2 \exp(-A_3/Kn_p) \right], \qquad (6)$$

where $\mu$ is the dynamic gas viscosity, $r_p$ is the radius of the particle, and $\Delta\mathbf{U}$ is the difference in velocity between the gas and the particle, respectively. For calculating $C_c$, the particle Knudsen number $Kn_p$ is defined as the ratio of the mean free path of the gas to the radius of the particles. The coefficients $A_1 = 1.231$, $A_2 = 0.4695$, and $A_3 = 1.1783$ were empirically obtained.[39] A further correction to this model for high Mach number flows was also provided.[23]

### 2. Molecular drag models

To reduce the dependence on empirical coefficients, analytically derived models were considered for the extremely rarefied regimes in this study. When the size of the nanoparticle is very small compared to the mean free path of the gas and gas atoms/molecules are specularly reflected from the surface of the nanoparticle, the drag force of the nanoparticle is[17]

$$\mathbf{F}_{\text{spec}} = \frac{4\pi}{3} r_p^2 N m \bar{c} \, \Delta\mathbf{U}. \qquad (7)$$

Alternatively, for diffusively reflected gas molecules, the drag force is

$$\mathbf{F}_{\text{diff}} = \left(1 + \frac{\pi}{8}\right) \frac{4\pi}{3} r_p^2 N m \bar{c} \, \Delta\mathbf{U}. \qquad (8)$$

Here, $N$ is the number density of the gas molecules, $m$ is the molecular mass of the gas, and $\bar{c}$ is the average speed of molecules in the gas, respectively. These models are well suited for low-speed flows, i.e., low Mach number flows ($Ma < 0.3$).

An analytical expression for both specularly and diffusively reflected atoms/molecules for intermediate and high-speed flows (high Mach numbers) is[18]

$$\mathbf{F}_{\text{spec}} = \frac{\pi^{3/2} \rho r_p^2 \bar{c}^2}{4} \left\{ \left(S + \frac{1}{2S}\right) \exp(-S^2) \right.$$
$$\left. + \sqrt{\pi}\left(S^2 + 1 - \frac{1}{4S^2}\right) \text{erf} \, S \right\}, \qquad (9)$$

$$\mathbf{F}_{\text{diff}} = \frac{\pi^{3/2} \rho r_p^2 \bar{c}^2}{4} \left\{ \left(S + \frac{1}{2S}\right) \exp(-S^2) \right.$$
$$\left. + \sqrt{\pi}\left(S^2 + 1 - \frac{1}{4S^2}\right) \text{erf} \, S + \frac{\pi S}{3} \right\}. \qquad (10)$$

Here, $\rho$ is the density of the gas and $S = \sqrt{\frac{m}{2k_B T}} \cdot \Delta\mathbf{U}$ denotes the molecular speed ratio, where $k_B$ is the Boltzmann constant and $T$ being the temperature of the gas. The total drag force on the particle is assumed to be a combination of a certain fraction ($\alpha$) of diffuse reflections and the remaining fraction ($1 - \alpha$) are specular reflections

$$\mathbf{F}_{\text{drag}} = (1 - \alpha) \, \mathbf{F}_{\text{spec}} + \alpha \, \mathbf{F}_{\text{diff}}. \qquad (11)$$

It is typically assumed that $\alpha = 0.9$,[17,40–42] which we used in the current work.

### 3. Relaxation of Epstein drag

For particles traversing across low-speed transition or molecular flow regimes (i.e., DSMC regions with $Kn_B > 0.05$), we observed by comparison with experimental data that the above-mentioned models overpredict the drag force in this regime due to the overestimation of impinging gas molecules that transfer momentum to the nanoparticle. Therefore, a relaxation of the drag force is necessary to accurately track particles in the flow by estimating the actual fraction of colliding molecules when particles move through a sub-cell of the simulation domain. For this purpose, a sub-cell of the flow field, in which a certain number of gas molecules exist, is considered. The gas velocity distribution functions in this sub-cell are assumed to follow the Maxwell–Boltzmann distribution. Like in DSMC, certain numbers of simulation molecules are created where each particle represents real molecules in the system that roughly have the same position and velocity. From the macroscopic flow data, such as pressure, flow velocity, and temperature, velocities are assigned to the simulation molecules in the sub-cell. The relative velocity of the randomly chosen simulation molecule with respect to the nanoparticle is estimated by:

$$\mathbf{u}_{r,i} = (\mathbf{u}_i + \mathbf{U}) - \mathbf{u}_p, \qquad (12)$$

where $\mathbf{u}_i$ is the thermal velocity of the randomly chosen simulation molecule from the Maxwell–Boltzmann distribution, $\mathbf{U}$ is the bulk velocity of the gas flow obtained from DSMC, and $\mathbf{u}_p$ is the velocity of the nanoparticle.

The collision between the nanoparticle and the impinging gas molecules that have a relative velocity less than the most probable speed of the gas molecules $\beta = \sqrt{2k_B T/m}$ in the low-speed high-Knudsen number regime is assumed stochastic. Thus, a gas molecule collides with the nanoparticle, if

$$1 - \exp\left(-\frac{|\mathbf{u}_{r,i}|}{\beta}\right) > R_f. \qquad (13)$$

Here, $R_f$ is a randomly generated number from $(0, 1]$ with a uniform distribution and Eq. (13) filters certain impinging molecules using Monte Carlo acception-rejection sampling. The fraction of colliding molecules $P_{\text{coll}}$ is determined per time step and the total drag force $\mathbf{F}_{\text{drag}}$ from Eq. (11) [obtained from Eqs. (7) and (8)] is relaxed accordingly

$$\mathbf{F}_{\text{drag, relaxed}} = P_{\text{coll}} \cdot \mathbf{F}_{\text{drag}}. \qquad (14)$$

### 4. Brownian motion

The drag force estimated above is the force obtained by averaging single collisions undergone by the particle per unit time, i.e., it is the mean force acting on the particle. However, the particle trajectory is also influenced by the Brownian motion due to the nanometer size range of the particle. The Brownian motion force is defined based on a Gaussian white noise random process having a spectral intensity $S_0$ as

$$\mathbf{F}_b = m_p \, \mathbf{G} \sqrt{\frac{\pi S_0}{\Delta t}}. \qquad (15)$$

Here, $\mathbf{G}$ is a vector of independent Gaussian random numbers with zero mean and unit variance and $\Delta t$ is the time step. For the drag
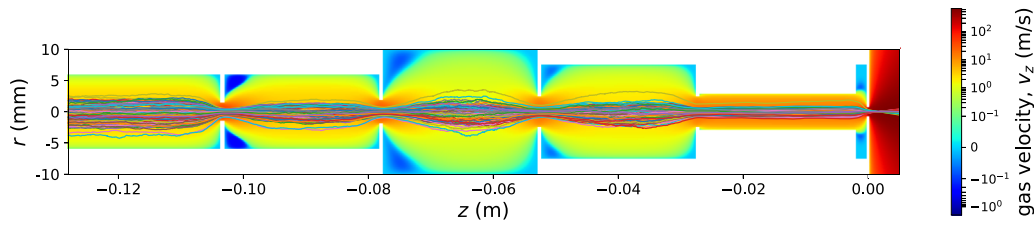
**FIG. 3.** Simulated trajectories (colored lines) of the 25 nm PS through the aerodynamic-lens stack drawn on top of the gas-flow field ($p_{in} = 150$ Pa) visualized by the axial velocity in a logarithmic color scale.

force modeled with the Stokes–Cunningham relation, the spectral intensity is defined as[43]

$$S_0 = \frac{27\,\mu\,k_B T}{4\,\pi^2\,r_p^5\,\rho_p^2\,C_c},\qquad(16)$$

where $\mu$ is the dynamic viscosity and $\rho_p$ the density of the particle, respectively. For the molecular drag force model, the spectral intensity is calculated as[44]

$$S_0 = \left(\frac{16}{3} + \frac{2\pi}{3}\sqrt{\frac{T_p}{T}}\right)\frac{\bar{c}}{2}\,p\,\frac{m}{m_p^2}\,r_p^2.\qquad(17)$$

Here, $T_p$ is the temperature of the particle and $p$ is the pressure of the gas, respectively. (For the effect of the Brownian motion, see Appendix A.)

## IV. RESULTS AND DISCUSSION

The numerical methodologies described in Sec. III are utilized to simulate the particle–beam evolution at different conditions presented in Table I. Figure 3 exemplarily shows the flow field and the corresponding nanoparticle trajectories throughout the computational domain for the 25 nm polystyrene spheres (PS) at an inlet pressure of $p_{in} = 150$ Pa. Here, $r$ represents the radial and $z$ being the axial coordinate of the flow domain. The flow field predicted by the hybrid

CFD–DSMC method is depicted by the axial velocity $v_z$ representing the main flow direction and the particle trajectories are calculated by molecular drag force models (Sec. III D 2).

The exit of the ALS is at $z = 0$. The flow domain defined by $z > 0$ represents the vacuum chamber, where the gas flow from the ALS expands at supersonic speeds. Figure 4(a) is the zoomed-in view of Fig. 3, which shows the simulated particle trajectories focusing (converge to a minimum beam width) and de-focusing inside the vacuum chamber. In the vacuum chamber, the particle beam widths are measured at different positions starting at $z = 1$ mm and onward. The particle beam evolving from the exit of the aerodynamic lens has a Gaussian-like distribution.[27] Therefore, the width of the particle beam is designated by the full-width at half-maximum (FWHM). The widths of the simulated particle beam at the corresponding experimental positions are compared with the experimental data in Fig. 4(b). In the current case, the beam profiles obtained by simulation show good agreement with the experimental data.

For every experimental case in Table I, $10^4$ particles were simulated with an initial radial velocity of $v_r = 0$ and an axial velocity following a normal distribution with a zero mean and a standard deviation of 10 m/s. The particles are positioned at the ALS inlet with a Gaussian distribution centered around $r = 0$ and FWHM of 0.0023 m. For particle numbers above 1000, the simulated beam profiles do not change significantly. Thus, with ten times more particles, it is ensured that the statistics are fully converged.



(a)



(b)
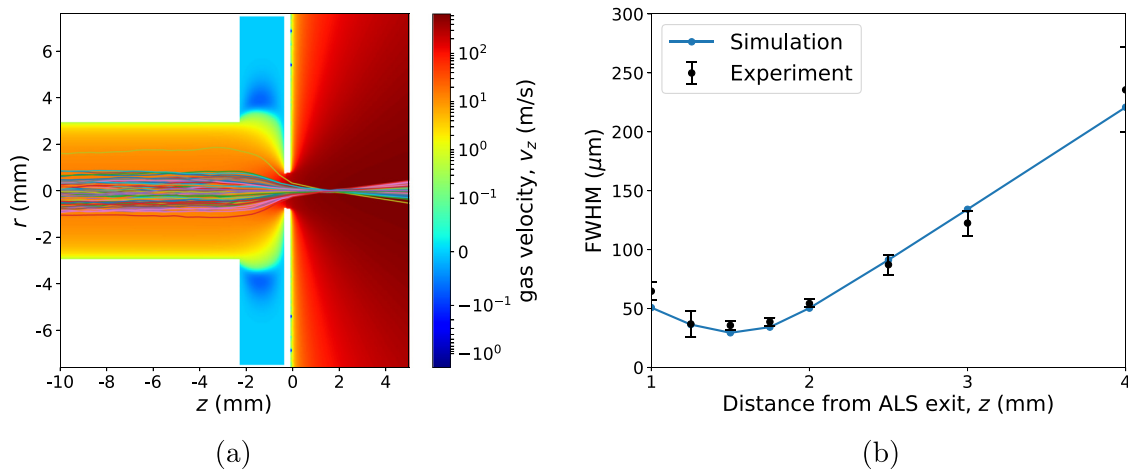
**FIG. 4.** (a) Zoom-in view of the ALS-exit into the high-vacuum chamber of Fig. 3, including simulated particle trajectories from the ALS exit into vacuum; (b) Particle-beam-size evolution (FWHM) of 25 nm PS at an inlet pressure of $p_{in} = 150$ Pa.

However, the level of accuracy of the simulation shown above highly depends on choosing the right modeling approach, which also varies for different experimental conditions, such as inlet pressure or particle size. Potential sources of error include experimental uncertainties – such as differences between the measured upstream pressure and the actual inlet pressure. For every test case, results are averaged and both the mean and standard deviation are estimated to quantify this uncertainty as shown in Fig. 4(b). Other sources of error include limitations in the numerical models (e.g., approximations in the drag force models and the flow modeling approach) and variations in boundary conditions. To ensure a reliable flow modeling approach, necessary steps have been taken to minimize these discrepancies through careful calibration of simulation parameters and sensitivity analyses. For details, refer to Peravali et al..[16]

In subsections IV A and IV B, the numerical approaches and models for the drag force mentioned in Sec. III are evaluated for different flow conditions by comparing the experimental particle beam evolution in the vacuum chamber with the simulated particle beam profile.

## A. Multi-scale regime

For the test cases having variable Knudsen number regimes, the flow field is simulated using the hybrid CFD/DSMC approach described

in Sec. III C. To understand where the transition from continuum to the rarefied regime takes place, Fig. 5(a) depicts the distribution of the breakdown Knudsen number $Kn_B$ in the vicinity of the ALS exit for an exemplary case from above. Obviously, for the case of the inlet pressure $p_{in} = 150$ Pa, the threshold of $Kn_B = 0.05$ is reached directly at the narrowest point of the outlet. Thus, the entire domain beyond the outlet has to be predicted via DSMC. Figures 5(b)–5(d) show what happens if the classical CFD solver is used in this region despite the violation of the continuum assumption. The largest deviations between the results predicted by pure CFD and the hybrid DSMC/CFD approach are visible for the temperature and the Mach number. For the hybrid method, large Ma numbers have reached 5 mm behind the ALS exit, whereas the CFD simulation predicts a sub-critical flow with $Ma < 1$. These large deviations in the flow field have to be taken into account when discussing the results of the particle trajectories.

Furthermore, a comparison of the computational costs reveals that the pure DSMC method is nearly 16 times more expensive than the hybrid DSMC/CFD approach, and its flow field exhibits higher statistical noise in low-Knudsen and low-Mach number regions, which necessitates additional simulations for statistical averaging and/or the use of more particles to filter out the noise, thereby further increasing the computational costs.
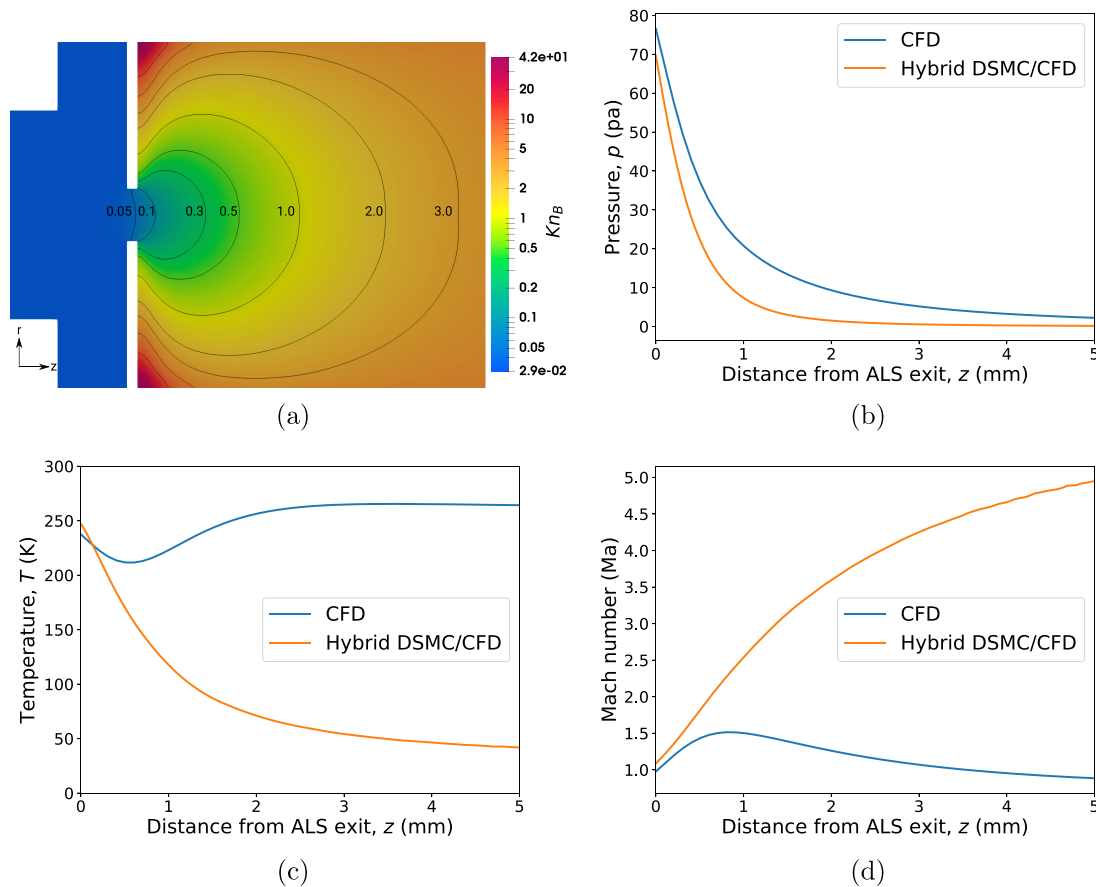


**FIG. 5.** (a) Continuum breakdown in the ALS depicted by the breakdown Knudsen number contour $Kn_B$ for an inlet pressure of $p_{in} = 150$ Pa; Comparison of the different distributions along the ALS centerline: (b) pressure; (c) temperature; (d) Mach number.
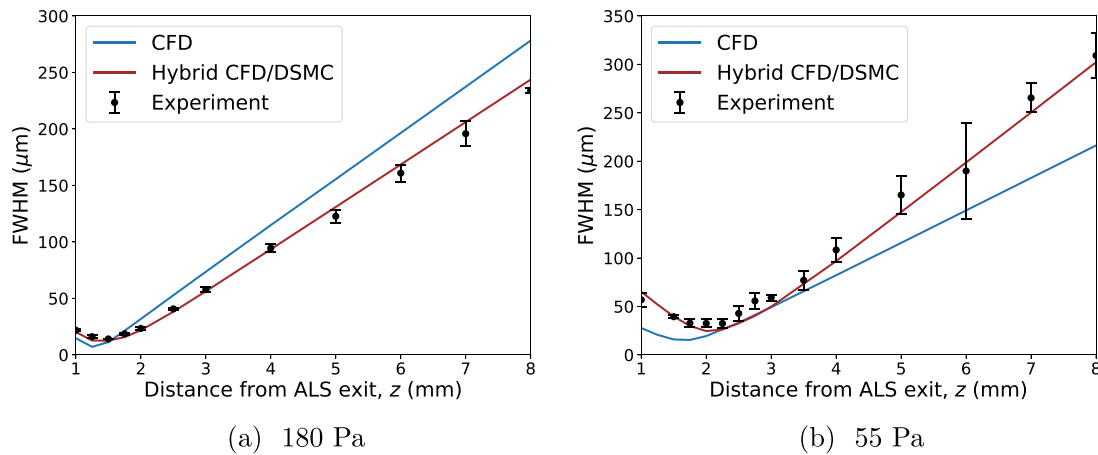
**FIG. 6.** Particle-beam-size evolution (FWHM) of 69 nm PS at two different inlet pressures.

The particle trajectories are subsequently predicted and evaluated like above for 69 and 42 nm PS. Since the test cases have very high particle Knudsen numbers (see Table I), the corresponding molecular drag force models are chosen based on the Mach number (*Ma*) of the flow. For $Ma < 0.3$, the Epstein[17] model [Eqs. (7) and (8)] is used and for $Ma > 0.3$, the drag model switches to Baines *et al.*[18] [Eqs. (9) and (10)]. However, it is observed that there are no significant deviations between the results achieved with these molecular drag models and the Stokes–Cunningham model (along with the correction to high Mach number flows[23])

Figures 6–8 show the particle beam widths at different positions behind the ALS exit for particle sizes of 69, 42, and 25 nm, respectively. The predicted data are given for different inlet pressures shown in Table I. The results predicted by the hybrid CFD/DSMC method show very good agreement with the experimental data for all particle sizes (i.e., focusing-defocusing behavior and focus position) compared with the pure CFD. This is due to the difference in flow fields predicted in the rarefied domain between the CFD and hybrid methods, as shown in the exemplary Fig. 5. The particle beam widths computed based on

the pure CFD code deviate significantly from the experiment as the inlet pressure reduces.

Accurately estimating the correct focus size and focus position is crucial for quantifying the efficiency of an ALS. Table II shows the differences in focus size ($w_{err}$) and focus position ($z_{err}$) relative to the experimental values for both the methods, CFD and hybrid CFD/DSMC. It clearly demonstrates the significant error reduction achieved by incorporating the hybrid approach. Overall, it is evident from Figs. 6–8 that the error associated with the hybrid CFD/DSMC approach falls well within the experimental uncertainty range, further supporting its validity.

Additionally, Appendix A shows a case with 25 nm gold nanoparticles (AuNP) where the hybrid DSMC–CFD methodology could predict the experimental trend quite well, too. Furthermore, the impact of Brownian diffusion on the beam widths is demonstrated. As visible, simulations without the Brownian force model [Eq. (17)] show a drastic reduction in beam widths, clearly indicating the necessity of Brownian diffusion in the model.
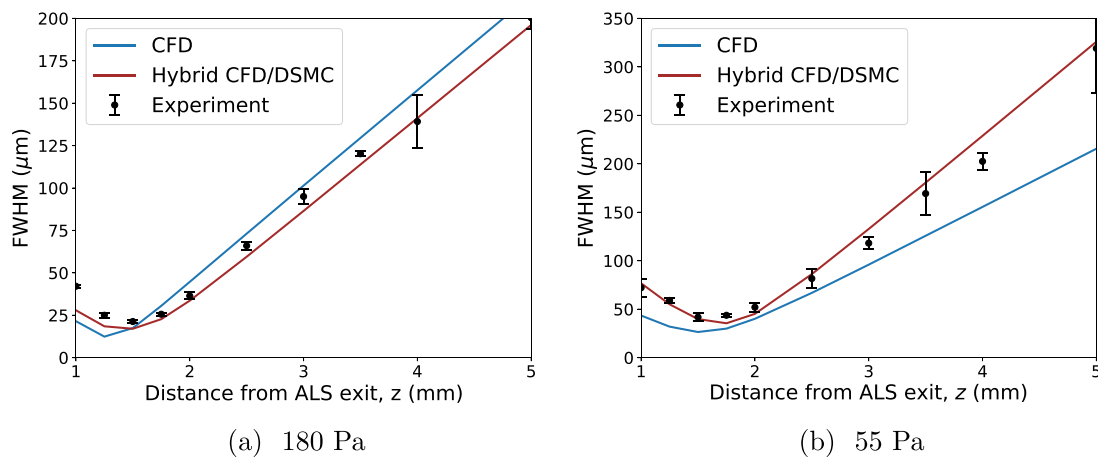


**FIG. 7.** Particle-beam-size evolution (FWHM) of 42 nm PS at two different inlet pressures.
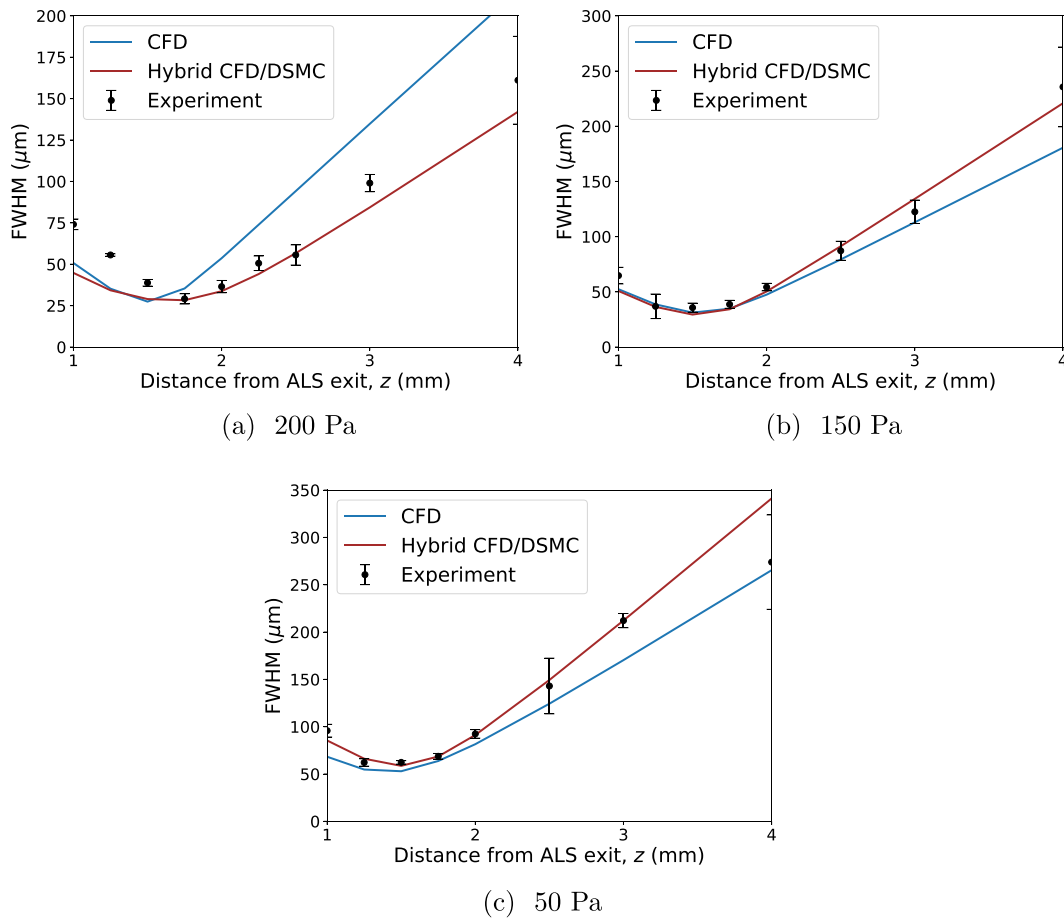
(a) 200 Pa



(b) 150 Pa



(c) 50 Pa

**FIG. 8.** Particle-beam-size evolution (FWHM) of 25 nm PS at three different inlet pressures.

## B. Highly rarefied regime

For the test cases with an inlet pressure of $p_{in} = 20$ Pa mentioned in Table I, the maximum global and local Knudsen numbers are evaluated to be greater than 0.1. Therefore, for these test cases, it is ideal to

**TABLE II.** Differences in focus size ($w_{err}$) and focus position ($z_{err}$) relative to the experimental values for various particle sizes and inlet pressures. The values are provided for both CFD and hybrid CFD/DSMC methods.

| Particle size (nm) | $p_{in}$ (Pa) | $w_{err}$ (%) | | $z_{err}$ (%) | |
|---|---|---|---|---|---|
| | | CFD | Hybrid | CFD | Hybrid |
| 69 | 180 | 49.57 | 9.21 | 16.66 | 0.0 |
| | 55 | 52.54 | 12.09 | 12.50 | 0.0 |
| 42 | 180 | 41.84 | 17.21 | 16.66 | 0.0 |
| | 55 | 36.76 | 14.98 | 16.66 | 0.0 |
| 25 | 200 | 5.73 | 2.80 | 14.28 | 0.0 |
| | 150 | 12.60 | 6.44 | 0.0 | 0.0 |
| | 50 | 11.99 | 6.41 | 0.0 | 0.0 |
| Average | | 30.1 | 9.9 | 11.0 | 0.0 |

use the pure DSMC approach. Nevertheless, Fig. 9 depicts a direct comparison between the pure CFD results and the DSMC data. The pressure and Mach number distributions along the ALS centerline and behind its exit are shown. As expected, the deviations are found to be even larger than in the multi-scale case discussed above. In the DSMC-predicted flow field, the flow reaches a sonic condition ($Ma = 1$) at the throat/ALS exit (commonly referred to as "choking"), a feature that is not captured by pure CFD in this regime. This circumstance has a significant impact on the evolution of the particle trajectories discussed below.

Once a smooth sampled flow field is established using DSMC, the particle trajectory calculations are carried out for 69 and 42 nm PS. Similar to the cases described in Sec. IV A, the corresponding molecular drag force models are chosen based on the Mach number of the flow [Eqs. (7)/(8) or Eqs. (9)/(10)]. Furthermore, the relaxed drag force model based on Monte Carlo sampling [Eq. (14)] described in Sec. III D 3 has also been used in place of the Epstein[17] model.

Figures 10(a) and 10(b) show the particle beam widths at different distances from the ALS exit for particle sizes of 69 and 42 nm, respectively. In addition to the pure DSMC method, for comparison purposes, the underlying flow fields are also simulated using pure CFD.
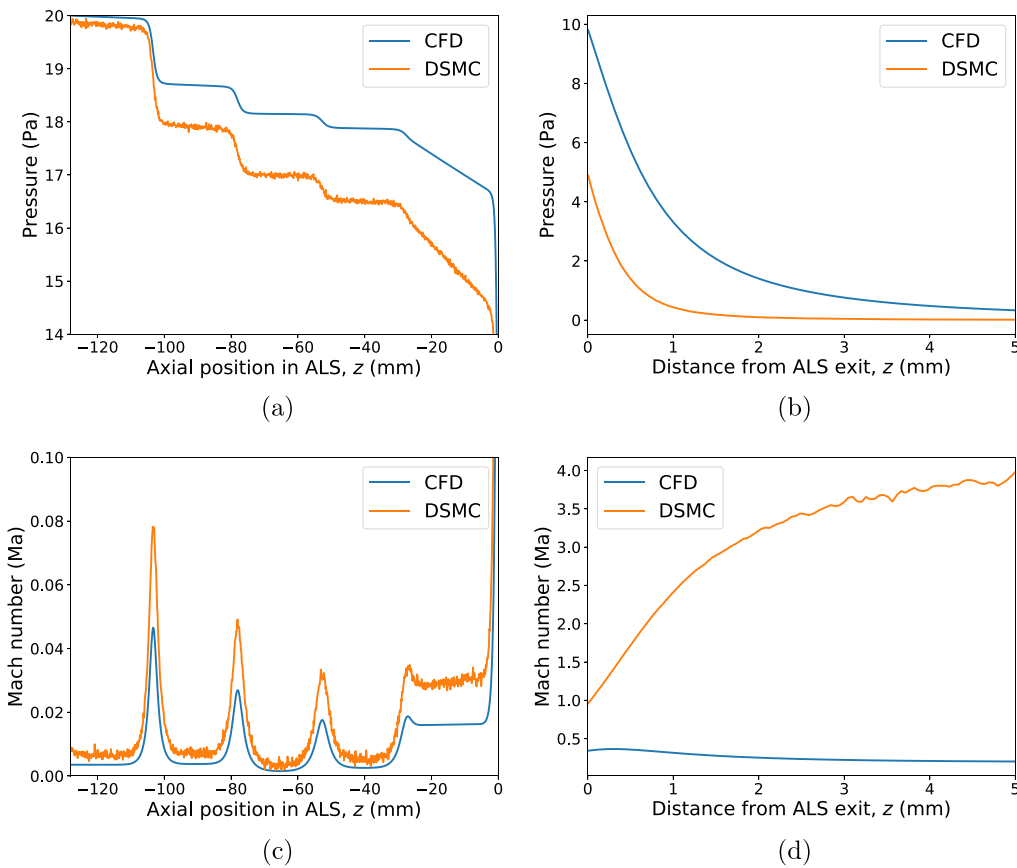
**FIG. 9.** Comparison of different distributions along the ALS centerline for the case of an inlet pressure $p_{in} = 20$ Pa: (a) pressure inside ALS; (b) pressure behind the exit of ALS; (c) Mach number inside ALS; (d) Mach number behind the exit of ALS.

The results predicted by CFD are not in good agreement with the experimental data for both particle sizes. Here, both the focus position and the width of the particle beam are underpredicted. According to the large deviations observed in the flow fields predicted by pure CFD (see Fig. 9), this outcome is not astonishing. In the case of DSMC, the particle beam evolution shows a similar trend as the experimental data, where the position of the focus is predicted in reasonable agreement with the measurements. However, the beam widths are
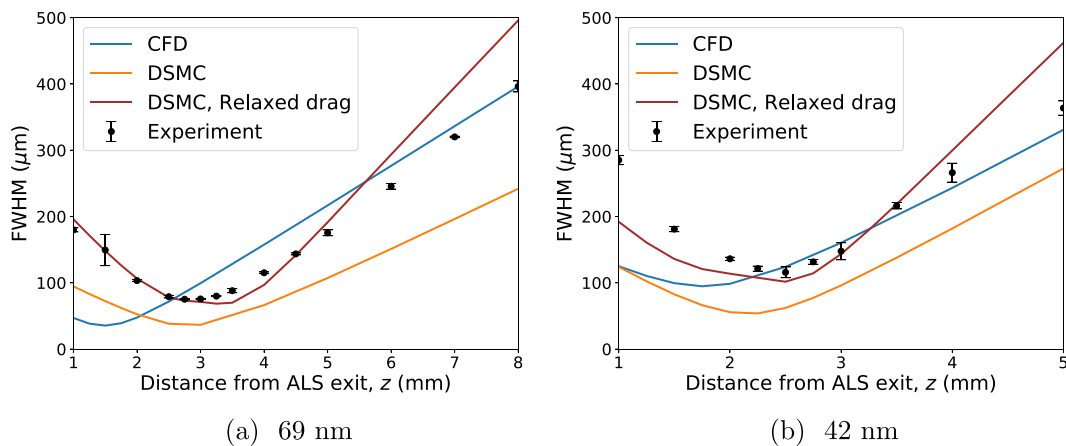


**FIG. 10.** Particle-beam-size evolution (FWHM) of PS at an inlet pressure of 20 Pa for two different particle sizes.

**TABLE III.** Differences in focus size ($w_{err}$) and focus position ($z_{err}$) relative to the experimental values for various particle sizes and inlet pressures. The values are provided for both CFD, DSMC and DSMC with relaxed drag model.

| Test case | $w_{err}$ (%) | | | $z_{err}$ (%) | | |
|---|---|---|---|---|---|---|
| | CFD | DSMC | DSMC relaxed | CFD | DSMC | DSMC relaxed |
| 69 nm PS | 53.14 | 51.54 | 2.92 | 45.45 | 8.3 | 4.16 |
| 42 nm PS | 18.92 | 48.88 | 16.28 | 40.0 | 10.0 | 0 |
| Average | 36.0 | 50.2 | 9.6 | 42.7 | 9.1 | 2.1 |

underpredicted due to overestimation of the drag force in this regime. Therefore, the molecular drag is relaxed according to Eqs. (13) and (14). Obviously, this corrected drag force yields a much better agreement with the experimental data for both particle sizes, predicting both the beam widths and the focus position quite well.

Table III summarizes the difference in focus size ($w_{err}$) and in focus position ($z_{err}$) relative to experimental values for predictions obtained using CFD, DSMC, and DSMC with a relaxed drag model. The table clearly demonstrates that the improved methodology (DSMC with relaxed drag model) substantially reduces the relative errors compared to the other approaches.

## V. CONCLUSIONS

We proposed and implemented an enhanced and accurate numerical methodology for the simulation of nanoparticle injection through aerodynamic lens systems. Our approach handles both the carrier gas flow through the system and the particle trajectories. For the former, a hybrid molecular-continuum simulation method was set up, which accounts for a wide range of Knudsen numbers in the flow fields of such lens systems, ranging from high-density gas to a highly rarefied flow during the expansion into the vacuum chamber.

Coupling CFD and DSMC allowed for limiting the use of the much more CPU-time intensive molecular model only to those regions, which cannot be accurately predicted by the continuum mechanics approach. For the prediction of the particle trajectories, drag force models from the literature were evaluated, including molecular drag models. For particles traversing through transitional regimes at the boundary between continuum and molecular flow, an additional correction factor was derived, taking into account the probability that a fraction of the molecules does not collide with a particle in a sub-cell.

The entire methodology was applied to nine different experimental configuration, three particle sizes and three inlet pressures, spanning a wide parameter space. In the multi-scale regime, the hybrid DSMC/CFD approach proves to be superior to the pure CFD method. No significant deviations between the results achieved with the molecular drag models and the Stokes–Cunningham model were observed. Quantitatively, the average relative error in the focus size was reduced from 30.1% with pure CFD to 9.9% with the hybrid method, while the relative error in the focus position decreased from about 12%–16% to nearly 0%. For the highly rarefied cases, the incorporation of DSMC with the relaxed drag model further decreased the errors, i.e., the average relative error in the focus size was reduced from 36.0 (using pure CFD) to 9.6, and the relative errors in the focus position decreased to 0% or 4.2%, respectively, thereby achieving excellent agreement with

the experimental data[27] – a performance unattainable by classical models. However, this model requires validation against different gas flow conditions, e.g., multi-species gas, and over a wide range of temperatures, 4–300 K, and particle sizes, 1–25 nm.

Despite these promising results, the methodology is not without limitations. Potential inaccuracies may arise in low-Mach number transitional flows within the DSMC regime, where high statistical errors in macroscopic quantities can occur. Additionally, for low-temperature (cryogenic) gas flows, quantum *ab initio* effects may become significant.[45] Moreover, the presence of vortices near the breakdown region might necessitate a two-way coupled hybrid CFD/DSMC coupling approach. The DSMC component can be a computational bottleneck for low-speed and transitional flows due to the increased number of simulations required to filter out statistical errors, and unsteadiness in the flow further intensifies the computational costs.

Future experiments are planned for improving the characterization of the relaxed drag force as well as for generating training data for the development of machine-learning models aimed at improving the semi-empirical drag models across a large range of flow conditions. Similarly, efforts will focus on improving heat transfer models that describe particle–gas interactions under varying collision dynamics.

## AUTHOR DECLARATIONS
### Conflict of Interest

The authors have no conflicts to disclose.

### Author Contributions

**Surya Kiran Peravali:** Formal analysis (equal); Investigation (lead); Methodology (equal); Software (lead); Validation (lead); Visualization (lead); Writing – original draft (lead); Writing – review & editing (lead). **Amit K. Samanta:** Conceptualization (supporting); Formal analysis (supporting); Investigation (supporting); Methodology (supporting); Supervision (supporting). **Muhamed Amin:** Conceptualization (supporting); Supervision (supporting). **Philipp Neumann:** Conceptualization (supporting); Methodology (supporting); Software (supporting); Supervision (supporting); Writing – original draft (supporting). **Jochen Küpper:** Conceptualization (supporting); Funding acquisition (equal); Investigation (supporting); Project administration (supporting); Supervision (equal); Writing –
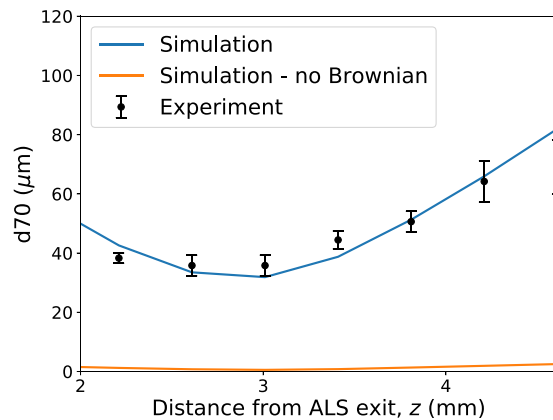
**FIG. 11.** Particle-beam-size evolution of 25 nm AuNP at inlet pressure of 180 Pa.

original draft (supporting); Writing – review & editing (supporting). **Michael Breuer:** Conceptualization (supporting); Formal analysis (supporting); Funding acquisition (equal); Investigation (supporting); Project administration (equal); Supervision (equal); Validation (supporting); Visualization (supporting); Writing – original draft (supporting); Writing – review & editing (supporting).

## DATA AVAILABILITY

The data that support the findings of this study are available within the article.

## APPENDIX A: ADDITIONAL CASE – FOCUSING OF 25 NM GOLD NANOMETER PARTICLES

In this section, an additional test case is presented. Figure 11 shows the particle beam width at different positions after the ALS exit for gold spheres of 25 nm at an inlet pressure of 180 Pa. For this gold–sphere case, a slightly different ALS geometry is used.[7] It has to be noted that for this setup, the beam width is quantified based on 70% quantile of particle positions in radial direction (d70) instead of FWHM. The hybrid CFD/DSMC approach is used along

with the molecular drag force model [Eqs. (7)/(8) or Eqs. (9)/(10) based on the Mach number of the flow]. As visible in Fig. 11, the results predicted by the simulation show very good agreement with the experimental data. Furthermore, the influence of Brownian diffusion [Eq. (17)] on the beam widths is also discussed. The simulation without the Brownian force model showed a drastic reduction in beam widths, clearly demonstrating the necessity of this model. This additional application case underlines the suitability of the chosen simulation approach.

## APPENDIX B: OTHER SUPPLEMENTARY INFORMATION

### 1. OpenFoam simulation

#### a. OpenFOAM mesh

For simulating gas flows through ALS geometries[7,27] using CFD, computational grids are generated using the `blockMesh` and `snappyHexMesh` utilities in OpenFoam. Since the ALS geometries are axisymmetric, structured body-fitted standard three-dimensional (3D) O-grid type grids are generated as shown in Fig. 12. The vacuum chamber in this simulation is represented by a cylindrical mesh of radius 5 mm and length of 10 mm from the exit of ALS ($z = 0$), respectively. Here, the wave transmissive outlet boundary condition is applied.[16]

The entire ALS mesh contains a total of approximately 2.44 $\times 10^6$ cells, which is based on grid-independence studies as shown in Fig. 13. In this grid study, the root mean square error (RMS error) of the ALS centerline velocity magnitude $\epsilon_U$ is calculated. By comparing results obtained by different grid resolutions with the reference simulation conducted with a fine grid consisting of $10 \times 10^6$ cells, it is obvious that the applied grid is appropriate.

#### b. Boundary conditions

In OpenFOAM, the computational domain is typically divided into patches, with boundary conditions applied as attributes to both the patches and the associated field variables. The OpenFOAM library offers a wide range of boundary condition types. Table IV summarizes the boundary conditions used in the present test cases.
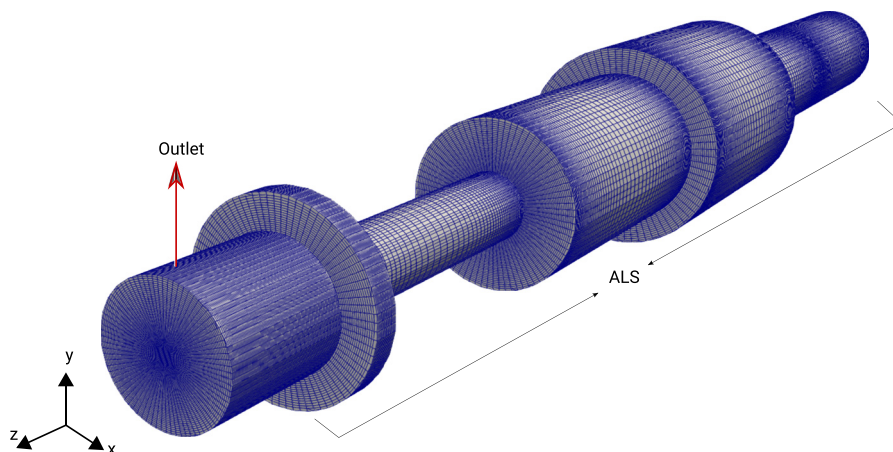


**FIG. 12.** Structured O-grid of the ALS geometry along with the vacuum chamber representation.
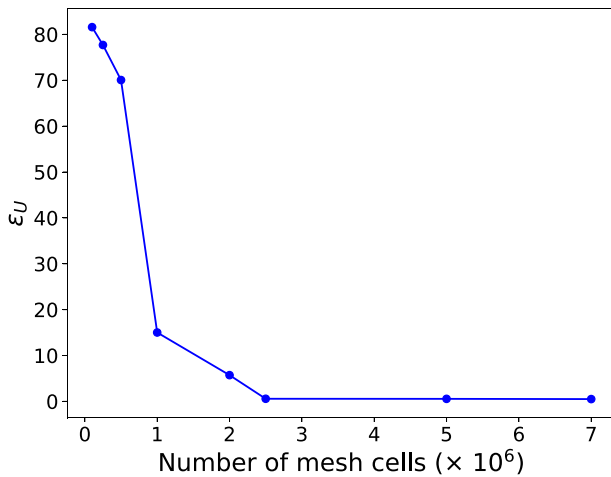
**FIG. 13.** Grid-independence study of the ALS grid.

**TABLE IV.** Boundary conditions for the ALS flow.

| Boundary | U | P | T |
|---|---|---|---|
| Inlet | zero gradient | fixed value | fixed value |
| Outlet | zero gradient | wave transmissive | zero gradient |
| Wall | no-slip | zero gradient | fixed value |

### 2. DSMC simulation

The DSMC simulator SPARTA[32] uses a Cartesian grid, unlike OpenFoam. To resolve the geometry of the ALS properly and to assure a grid that fits the entire range of flow Knudsen numbers, a regular grid of size $\Delta x = 5 \times 10^{-5}$ m is used. The time step $\Delta t$ used in the simulation is calculated by $\Delta t = 0.7 \, \Delta x / \bar{v}$, where $\bar{v} = \sqrt{8 k_B T / (\pi m)}$ is the mean thermal speed of the gas molecules. This calculation yields an approximate time step of $1 \times 10^{-7}$ s. The fully diffusive (isotropic scattering) gas–surface interaction model is used to model the interaction between ALS walls and the gas. The no-time-counter (NTC) method is employed for collision sampling along with VSS molecular model. The Larsen and Borgnakke model with constant relaxation is applied to handle the internal energy exchange.[16] The number of DSMC particles per grid cell $N_c \approx 1650$ is used, and the number of sampling time steps $N_T$ used was 40 000, thereby giving a sample size $S = N_c \times N_T = 66 \times 10^6$.

### REFERENCES

[1]R. Neutze, R. Wouts, D. van der Spoel, E. Weckert, and J. Hajdu, "Potential for biomolecular imaging with femtosecond X-ray pulses," Nature **406**, 752–757 (2000).

[2]J. C. Spence and H. N. Chapman, "The birth of a new field," Philos. Trans. R. Soc. B **369**, 20130309 (2014).

[3]T. Ekeberg, M. Svenda, C. Abergel, F. R. N. C. Maia, V. Seltzer, J.-M. Claverie, M. Hantke, O. Jönsson, C. Nettelblad, G. van der Schot, M. Liang, D. P. DePonte, A. Barty, M. M. Seibert, B. Iwan, I. Andersson, N. D. Loh, A. V. Martin, H. Chapman, C. Bostedt, J. D. Bozek, K. R. Ferguson, J. Krzywinski, S. W. Epp, D. Rolles, A. Rudenko, R. Hartmann, N. Kimmel, and J. Hajdu,

"Three-dimensional reconstruction of the giant mimivirus particle with an X-ray free-electron laser," Phys. Rev. Lett. **114**, 098102 (2015).

[4]M. Seibert, T. Ekeberg, F. Maia, M. Svenda, J. Andreasson, O. Jönsson, D. Odić, B. Iwan, A. Rocker, D. Westphal, M. Hantke, D. DePonte, A. Barty, J. Schulz, L. Gumprecht, N. Coppola, A. Aquila, M. Liang, T. White, and J. Hajdu, "Single mimivirus particles intercepted and imaged with an X-ray laser," Nature **470**, 78–81 (2011).

[5]K. Ayyer, P. L. Xavier, J. Bielecki, Z. Shen, B. J. Daurer, A. K. Samanta, S. Awel, R. Bean, A. Barty, M. Bergemann, T. Ekeberg, A. D. Estillore, H. Fangohr, K. Giewekemeyer, M. S. Hunter, M. Karnevskiy, R. A. Kirian, H. Kirkwood, Y. Kim, J. Koliyadu, H. Lange, R. Letrun, J. Lübke, T. Michelat, A. J. Morgan, N. Roth, T. Sato, M. Sikorski, F. Schulz, J. C. H. Spence, P. Vagovic, T. Wollweber, L. Worbs, O. Yefanov, Y. Zhuang, F. R. N. C. Maia, D. A. Horke, J. Küpper, N. D. Loh, A. P. Mancuso, and H. N. Chapman, "3D diffractive imaging of nano-particle ensembles using an x-ray laser," Optica **8**, 15–23 (2021).

[6]N. Roth, D. A. Horke, J. Lübke, A. K. Samanta, A. D. Estillore, L. Worbs, N. Pohlman, K. Ayyer, A. Morgan, H. Fleckenstein, M. Domaracky, B. Erk, C. Passow, J. Correa, O. Yefanov, A. Barty, S. Bajt, R. A. Kirian, H. N. Chapman, and J. Küpper, "New aerodynamic lens injector for single particle diffractive imaging," Nucl. Instrum. Methods Phys. Res, Sect. A **1058**, 168820 (2024).

[7]L. Worbs, N. Roth, J. Lübke, A. D. Estillore, P. L. Xavier, A. K. Samanta, and J. Küpper, "Optimizing the geometry of aerodynamic lens injectors for single-particle coherent diffractive imaging of gold nanoparticles," J. Appl. Crystallogr. **54**, 1730–1737 (2021).

[8]X. Zhang, K. A. Smith, D. R. Worsnop, J. Jimenez, J. T. Jayne, and C. E. Kolb, "A numerical characterization of particle beam collimation by an aerodynamic lens-nozzle system: Part I. An individual lens or nozzle," Aerosol Sci. Technol. **36**, 617–631 (2002).

[9]X. Zhang, K. A. Smith, D. R. Worsnop, J. L. Jimenez, J. T. Jayne, C. E. Kolb, J. Morris, and P. Davidovits, "Numerical characterization of particle beam collimation: Part II. Integrated aerodynamic-lens–nozzle system," Aerosol Sci. Technol. **38**, 619–638 (2004).

[10]X. Wang, F. E. Kruis, and P. H. McMurry, "Aerodynamic focusing of nanoparticles: I. Guidelines for designing aerodynamic lenses for nanoparticles," Aerosol Sci. Technol. **39**, 611–623 (2005).

[11]X. Wang, A. Gidwani, S. Girshick, and P. McMurry, "Aerodynamic focusing of nanoparticles: II. Numerical simulation of particle motion through aerodynamic lenses," Aerosol Sci. Technol. **39**, 624–636 (2005).

[12]X. Wang and P. H. McMurry, "A design tool for aerodynamic lens systems," Aerosol Sci. Technol. **40**, 320–334 (2006).

[13]N. Roth, S. Awel, D. A. Horke, and J. Küpper, "Optimizing aerodynamic lenses for single-particle imaging," J. Aerosol Sci. **124**, 17–29 (2018).

[14]S. Welker, M. Amin, and J. Küpper, "CMInject: Python framework for the numerical simulation of nanoparticle injection pipelines," Comput. Phys. Commun. **270**, 108138 (2022).

[15]E. Cunningham and J. Larmor, "On the velocity of steady fall of spherical particles through fluid medium," Proc. R. Soc. London, Ser. A **83**, 357–365 (1910).

[16]S. K. Peravali, V. Jafari, A. K. Samanta, J. Küpper, M. Amin, P. Neumann, and M. Breuer, "Accuracy and performance evaluation of low density internal and external flow predictions using CFD and DSMC," Comput. Fluids **279**, 106346 (2024).

[17]P. S. Epstein, "On the resistance experienced by spheres in their motion through gases," Phys. Rev. **23**, 710–733 (1924).

[18]M. J. Baines, I. P. Williams, A. S. Asebiomo, and R. L. Agacy, "Resistance to the motion of a small sphere moving through a gas," Mon. Not. R. Astron. Soc. **130**, 63–74 (1965).

[19]C. B. Henderson, "Drag coefficients of spheres in continuum and rarefied flows," AIAA J. **14**, 707–708 (1976).

[20]E. Loth, "Compressibility and rarefaction effects on drag of a spherical particle," AIAA J. **46**, 2219–2228 (2008).

[21]R. S. C. Davuluri, S. C. C. Bailey, K. A. Tagavi, and A. Martin, "A drag coefficient model for Lagrangian particle dynamics relevant to high-speed flows," Int. J. Heat Fluid Flow **87**, 108706 (2021).

[22]C. Li, N. Singh, A. Andrews, B. A. Olson, T. E. Schwartzentruber, and C. J. Hogan, "Mass, momentum, and energy transfer in supersonic aerosol deposition processes," Int. J. Heat Mass Transfer **129**, 1161–1171 (2019).

[23]N. Singh, M. Kroells, C. Li, E. Ching, M. Ihme, C. J. Hogan, and T. E. Schwartzentruber, "General drag coefficient for flow over spherical particles," AIAA J. **60**, 587–597 (2022).

[24]M. A. Gallis, J. R. Torczynski, and D. J. Rader, "An approach for simulating the transport of spherical particles in a rarefied gas flow via the direct simulation Monte Carlo method," Phys. Fluids **13**, 3482–3492 (2001).

[25]J. Burt, "Monte Carlo simulation of solid rocket exhaust plumes at high altitude," Ph.D. thesis (University of Michigan, 2006).

[26]D. E. Rothe, "Experimental study of viscous low-density nozzle flows," Report No. CAL-AI-2590-A-2 (Cornell Aeronautical Laboratory, Inc., Cornell University, Buffalo, NY, 1970).

[27]L. Worbs, "Toward cryogenic beams of nanoparticles and proteins," Ph.D. thesis (Universität Hamburg, Hamburg, Germany, 2022).

[28]S. Awel, R. A. Kirian, N. Eckerskorn, M. Wiedorn, D. A. Horke, A. V. Rode, J. Küpper, and H. N. Chapman, "Visualizing aerosol-particle injection for diffractive-imaging experiments," Opt. Express **24**, 6507–6521 (2016).

[29]ESI-OpenCFD, see https://www.openfoam.com for "OpenFOAM - The Open Source CFD Toolbox," version v2112 (2004).

[30]F. M. White, *Viscous Fluid Flow* (McGraw-Hill, 2006).

[31]G. A. Bird, *Molecular Gas Dynamics and Direct Simulation of Gas Flows* (Oxford, 1994).

[32]Sandia Corporation, *Sparta Users Manual* (Sandia National Laboratories, 2022).

[33]I. Boyd, "Predicting breakdown of the continuum equations under rarefied flow conditions," AIP Conf. Proc. **663**, 899–906 (2003).

[34]M. Pfeiffer, A. Mirza, and P. Nizenkov, "Evaluation of particle-based continuum methods for a coupling with the direct simulation Monte Carlo method based on a nozzle expansion," Phys. Fluids **31**, 073601 (2019).

[35]F. La Torre, S. Kenjeres, C. R. Kleijn, and J.-L. P. A. Moerel, "Evaluation of micronozzle performance through DSMC, Navier-Stokes and coupled DSMC/ Navier-Stokes approaches," in *9th International Conference on Computational Science (ICCS 2009)*, Baton Rouge, LA, May 25–27 (Springer, 2009), Part I 9, pp. 675–684.

[36]D. E. R. Espinoza, V. Casseau, T. J. Scanlon, and R. E. Brown, "An open-source hybrid CFD-DSMC solver for high speed flows," AIP Conf. Proc.**1786**, 050007 (2016).

[37]M. Alletto and M. Breuer, "One–way, two–way and four–way coupled LES predictions of a particle–laden turbulent flow at high mass loading downstream of a confined bluff body," Int. J. Multiphase Flow **45**, 70–90 (2012).

[38]M. Breuer and M. Alletto, "Efficient simulation of particle–laden turbulent flows with high mass loadings using LES," Int. J. Heat Fluid Flow **35**, 2–12 (2012).

[39]D. K. Hutchins, M. H. Harper, and R. L. Felder, "Slip correction measurements for solid spherical particles by modulated dynamic light scattering," Aerosol Sci. Technol. **22**, 202–218 (1995).

[40]R. A. Millikan, "Coefficients of slip in gases and the law of reflection of molecules from the surfaces of solids and liquids," Phys. Rev. **21**, 217–238 (1923).

[41]R. A. Millikan, "The general law of fall of a small spherical body through a gas, and its bearing upon the nature of molecular reflection from surfaces," Phys. Rev. **22**, 1–23 (1923).

[42]M. Allen and O. Raabe, "Re-evaluation of Millikan's oil drop data for the motion of small particles in air," J. Aerosol Sci. **13**, 537–547 (1982).

[43]A. Li and G. Ahmadi, "Dispersion and deposition of spherical particles from point sources in a turbulent channel flow," Aerosol Sci. Technol. **16**, 209–226 (1992).

[44]N. Roth, M. Amin, A. K. Samanta, and J. Küpper, "Microscopic force for aerosol transport," arXiv:2006.10652 (2020).

[45]F. Sharipov, "Modeling of transport phenomena in gases based on quantum scattering," Physica A **508**, 797–805 (2018).